



Novel cerium doped titania catalysts for photocatalytic decomposition of ammonia



Martin Reli^{a,*}, Nela Ambrožová^b, Marcel Šihor^a, Lenka Matějová^c, Libor Čapek^d,
Lucie Obalová^{a,b}, Zdeněk Matěj^e, Andrzej Kotarba^f, Kamila Kočí^{a,g}

^a Institute of Environmental Technology, VSB-Technical University of Ostrava, 17. listopadu 15/2172, Ostrava 708 33, Czech Republic

^b Department of Physical Chemistry and Theory of Technological Processes, Faculty of Metallurgy and Materials Engineering, VSB-Technical University of Ostrava, 17. listopadu 15/2172, Ostrava 708 33, Czech Republic

^c Nanotechnology Centre, VSB-Technical University of Ostrava, 17. listopadu 15/2172, Ostrava 708 33, Czech Republic

^d Department of Physical Chemistry, Faculty of Chemical Technology, University of Pardubice, Studentská 573, Pardubice 532 10, Czech Republic

^e Department of Condensed Matter Physics, Faculty of Mathematics and Physics, Charles University in Prague, Ke Karlovu 5, Prague 121 16, Czech Republic

^f Faculty of Chemistry, Jagiellonian University, Ingardena 3, Krakow 30 060, Poland

^g Energy Units for Utilization of non Traditional Energy Sources, VSB-Technical University of Ostrava, 17. listopadu 15/2172, Ostrava 708 33, Czech Republic

ARTICLE INFO

Article history:

Received 13 July 2014

Received in revised form 31 August 2014

Accepted 7 October 2014

Available online 19 October 2014

Keywords:

Cerium TiO₂ nanoparticles

Photocatalysis

Ammonia decomposition

ABSTRACT

Parent TiO₂ and cerium doped TiO₂ photocatalysts (with cerium loadings in the range 0.6–1.4 wt.%) were prepared by using the sol–gel method controlled within reverse micelles of nonionic surfactant Triton X-114 in cyclohexane. Textural, structural, microstructural, optical and electronic properties of photocatalysts were characterized in detail by using nitrogen physisorption, powder X-ray diffraction, diffuse reflectance UV–vis spectroscopy and contact potential difference measurements. It was proved that increasing amount of cerium ions in TiO₂ decreases the anatase crystallites size, which corresponded to the increase of specific surface area of the catalysts. The shift of spectral response of cerium doped catalysts to the visible light region was also observed, the significant decrease of absorption edge of photocatalysts with increasing Ce loading within 0.6–1.4 wt.% was detected. The photocatalytic decomposition of ammonia was carried out in a stirred batch annular reactor and the main product was hydrogen. The energetics of the TiO₂ photocatalysts, which were crucially affected by the doping with Ce ions, play the key role in the ammonia photocatalytic decomposition.

© 2014 Elsevier B.V. All rights reserved.

1. Introduction

Ammonia is a common water contaminant with strong effects on environment and human health. The term ammonia includes nonionized form (NH₃) and the ammonium cation (NH₄⁺) unless stated otherwise. Ammonia is mostly used in fertilizers and animal feed production and in the manufacture of fibers, plastics, explosives, paper and rubber. It is an important pollutant containing nitrogen and source of nutrients that may accelerate the eutrophication and cause algal growth in natural water. Natural levels in groundwater and surface water are usually below 0.2 mg/l. The threshold odor concentration of ammonia in water is approximately 1.5 mg/l.

Disposal of ammonia contaminated waters, no matter what origin, is not a trivial. Several methods have been developed and

applied for the treatment of ammonia-containing wastewater, including biological processes, air stripping, ion exchange, breakpoint chlorination, and chemical oxidation [1,2]. Among these methods, biological processes are generally regarded to be the most efficient. However, these processes have disadvantages, including handling difficulties and large equipment requirements. Moreover, they are difficult to apply for the treatment of wastewater that contains for bacteria harmful co-existing species [3].

The photocatalytic reaction seems to be the right way for decreasing ammonia concentrations in waste water. The most of studies have concerned on ammonia photocatalytic oxidation to possible products such as N₂, N₂O, NO₂, NO₃[−] over titanium dioxide [4–10], TiO₂ perlite [11], TiO₂/LECA (light expanded clay aggregate) [12,13], platinum loaded titanium dioxide [3,14–16], titanate nanotube [17,18], and Cu/TiO₂/SiO₂ modified with nitrogen [19].

On the contrary, only a few studies focused on the photocatalytic ammonia decomposition to nitrogen and hydrogen. Li et al. [20] investigated photodecomposition of ammonia over NiO and RuO₂ loaded SrTiO₃ and BaTiO₃. Nemoto et al. [21] reported about

* Corresponding author. Tel.: +420 597 327 319.

E-mail address: martin.reli@vsb.cz (M. Reli).

optimum platinum loading TiO₂ and reaction pH for the photocatalytic decomposition of ammonia in aqueous solution. Kominami et al. [22] studied NH₃ photocatalytic decomposition over metal-loaded TiO₂ (Pt, Pd, Au, Ag, Cu, Ir). The best catalyst for this reaction was platinum-loaded TiO₂. Yazawa et al. [23] investigated reaction mechanism of ammonia decomposition to nitrogen and hydrogen over metal loaded titanium dioxide photocatalyst. The photo-formed hole on the titanium oxide oxidizes NH₃ to form amide radical ($\cdot\text{NH}_2$) and proton. The amide radicals produce hydrazine (N₂H₄), and it can be further decomposed to form nitrogen and hydrogen. They also investigated the addition of different metals – Pt, Rh, Pd, Au, Ni, Cu – to titanium dioxide and found out Pt/TiO₂ photocatalyst exhibited the best activity.

There is also another important advantage in the photocatalytic NH₃ decomposition. Ammonia is attracting great attention as a possible energy source due to production of hydrogen from its decomposition.

To best of our knowledge, cerium modified TiO₂ has never been tested for the photocatalytic decomposition of ammonia. We used cerium doped TiO₂ in our previous work [24] where the influence of different amount of cerium (0.6 wt.%–21.1 wt.%) on the yields of the photocatalytic reduction of carbon dioxide was tested. Based on experimental data, it was found out that the addition of cerium lowers the band gap of the photocatalyst. The most efficient catalyst was the one with the lowest amount of cerium (0.6 wt.%). In this case the band gap was lowered and also the excited electrons had potential high enough to reduce H⁺/H₂. Therefore, the series of cerium doped TiO₂ with lower amounts of cerium (0.6–1.4 wt.%) were prepared for further research.

This work succeeds the previous one on similar systems [24]. The correlation between the catalysts photoactivity, the energies of band gap and the energies of holes and electrons formation will be further discussed. In this case, the photocatalytic decomposition of ammonia was chosen as a model reaction. Ammonium hydroxide was chosen as the ammonia source.

2. Experimental

2.1. Preparation of cerium doped TiO₂ photocatalysts

The parent TiO₂ and a set of cerium doped TiO₂ photocatalysts with 0.6–1.4 wt.% of Ce were prepared via sol–gel processing controlled within reverse micelles of nonionic surfactant Triton X-114 in cyclohexane in combination with calcination [25,26]. Titanium(IV) isopropoxide (Ti(OCH(CH₃)₂)₄, purity >97%, Aldrich) and cerium(III) nitrate hexahydrate (Ce(NO₃)₃·6H₂O, Aldrich) were used as metal cations sources. For TiO₂ synthesis, the molar ratio of cyclohexane: Triton X-114:H₂O:Ti(OCH(CH₃)₂)₄ was kept 11:1:1:1 [25]. For the synthesis of Ce-doped TiO₂ (0.6, 1.2 and 1.4 wt.% of Ce), the molar ratio of cyclohexane: Triton X-114:H₂O:Ce(NO₃)₃·6H₂O+Ti(OCH(CH₃)₂)₄ was also 11:1:1:1, the appropriate amount of Ce(NO₃)₃·6H₂O was always dissolved using 3.5 ml of anhydrous ethanol [26]. The prepared homogeneous transparent sols were poured in a thin layer on Petri's dishes and left for 48 h on air at ambient temperature and pressure for gelation. The sols converted into rigid transparent yellow-colored gels. The titania and cerium doped titania gels were thermally treated at 350 °C for 4 h and then up to 500 °C for another 2 h with heating rate 3 °C/min in order to produce powder photocatalysts. All prepared solids were sieved to the particle size <0.160 mm.

2.2. Characterization of photocatalysts

Chemical analysis of powder catalysts was done on an ARL 9400 XP sequential WD-XRF spectrometer. All peak intensity data were

collected under vacuum conditions using the software WinXRF. The analyzed powders were pressed into pellets about 0.6 mm thick and the diameter of 25 mm without any binding agent and covered with 4 μm supporting polypropylene film.

Nitrogen physisorption was performed on the automated volumetric apparatus NOVA2000e (Quantachrome Instruments, USA) after sample degassing at 105 °C for 24 h under the vacuum less than 1 Torr. The adsorption–desorption isotherms of nitrogen were measured at –196 °C. The specific surface area, S_{BET}, was calculated according to the classical Brunauer–Emmett–Teller (BET) theory for the p/p_0 range = 0.05–0.30 [27,28].

XRD powder diffraction patterns were measured using PANalytical MPD diffractometer in the conventional Bragg–Brentano setup, using Ni-filtered CuKα radiation, variable divergence and antiscatter slits, 0.04 rad axial Soller slits and PIXcel detector. NIST LaB₆ standard reference material (660a) was used for the instrumental broadening calibration. XRD data analysis, focused on determination of lattice parameters/cell volume and crystallite size, was done using the Rietveld/WPPM [29] implemented in the software MSTRUCT [30,31]. Models described in [32] were used.

UV–vis diffuse reflectance spectra of hydrated and granulated (0.25–0.50 mm) catalysts were measured in quartz cuvettes (thickness 5 mm) by using a GBS CINTRA 303 spectrometer (GBC Scientific Equipment, Australia) equipped with an integrating sphere covered by BaSO₄ layer as a standard. The spectra were recorded in the range of the wavelengths 200–900 nm (lamps switched at 350 nm) and the scan rate was 100 nm/min. The scan step was 1 nm and the width of monochromator slit was 2 nm. The reflectances were recalculated to the absorption using the Kubelka–Munk equation:

$$F(R_{\infty}) = (1 - R_{\infty})^2 / 2 \cdot R_{\infty}, \quad (1)$$

where R_{∞} is the diffuse reflectance from a semi-infinite layer.

The contact potential difference (V_{CPD}) measurements were carried out by the dynamic condenser method of Kelvin with a KP6500 probe (McAllister Technical Services). The reference electrode was a standard stainless steel plate with diameter of 3 mm ($\Phi_{\text{ref}} = 4.3$ eV) provided by the manufacturer. During the measurements, the gradient of the peak-to-peak versus backing potential was set to 0.2, whereas the vibration frequency and amplitude was set to 120 Hz and 40 a.u. The final V_{CPD} value was an average of 60 independent points using two backing potentials. The measurements were carried out under atmospheric pressure and ambient temperature. Before the measurements the samples were pressed into pellets of 10 mm diameter using the 8 MPa pressure. The work function values were obtained from a simple relation $V_{\text{CPD}} = \Phi_{\text{ref}} - \Phi_{\text{sample}}$.

2.3. Photocatalytic tests

The photocatalytic decomposition of ammonia was carried out in a stirred batch annular reactor with a suspended catalyst illuminated by UV 8 W Hg pen-ray lamp with a peak intensity at 254 nm (Ultra-Violet Products Inc., USA, 11SC-1) situated in the center of the quartz glass tube. The reactor shell was made from stainless steel (Fig. 1). Ammonium hydroxide was chosen as the source of ammonia. The concentration of ammonia was 0.883 g/l. To create an inert atmosphere in the reactor and to remove soluble oxygen and nitrogen, argon (purity 5.0) was bubbled through the suspension. Due to this purging the concentration of ammonia decreased to 0.8274 g/l. The gas samples were discontinuously taken and H₂ and CH₄ were immediately analyzed on a gas chromatograph equipped with a TCD and FID (YL 6000 Young-Lin, Labicom). The columns used for the separation were Pora-plot Q and MolSieve. Another gas chromatograph (Agilent 7890 equipped with MolSieve column) was used for analyzing nitrous oxide which might be a possible product.

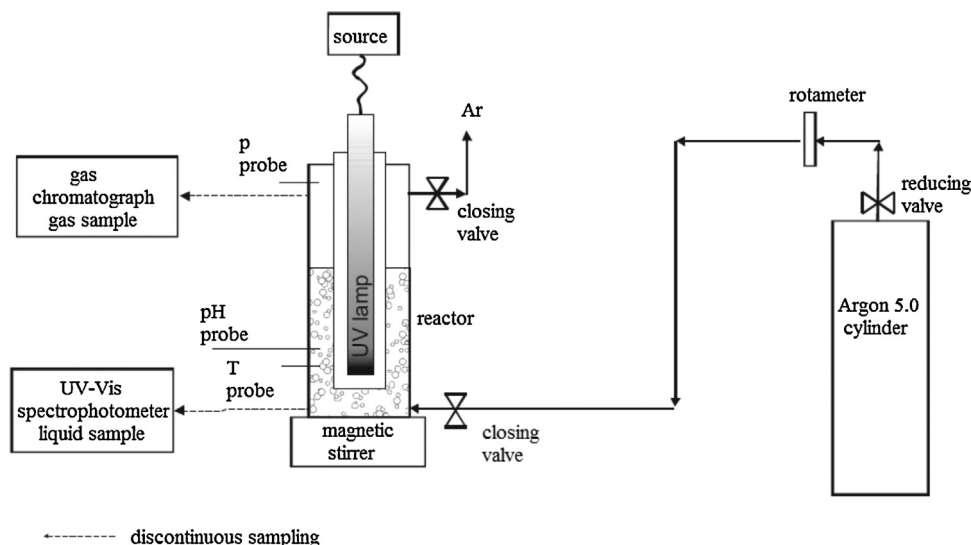


Fig. 1. The block scheme of the set-up for the photocatalytic decomposition of ammonia.

The concentration of ammonia was measured on UV–vis spectrophotometer (Specord 250 PLUS) against blank (without ammonia). Measurements were conducted at wavelength 405 nm. Shortly before analysis 2 ml of Nessler reagent were added to the sample (sample turned orange).

It was important to minimize the influence of the transport phenomena during kinetic measurements. Therefore, the catalyst loading 1 g/dm^3 was chosen to avoid concentration gradients in the bulk of stirred suspension due to the light scattering effect caused by high solid phase concentration [33,34]. The determination of suitable volume of the liquid phase in the annular photoreactor to fulfill the requirements of perfect mixing has been found to be 100 ml [35].

All data were measured twice. The accuracy of measurements was verified by series of repeated experiments and the relative error of hydrogen yields was lower than 10%.

The blank reactions were also performed to ensure that the hydrogen production was due to the photodecomposition of ammonia.

3. Results and discussion

3.1. Photocatalysts characterization

All prepared photocatalysts were characterized by several techniques in order to determine their physicochemical, optical and electronic properties which could contribute to explanation of their photoactivity for the photocatalytic decomposition of ammonia.

3.2. Chemical composition and surface area

The real cerium amounts (in wt.%) in Ce-doped titania photocatalysts and specific surface areas (S_{BET}) of all prepared photocatalysts along with commercial TiO_2 Evonik P25 are summarized in Table 1. It can be easily noticed that the addition of cerium within 0–1.4 wt.% leads to the monotonous increase of the specific surface area of prepared photocatalysts. The biggest increase to $76 \text{ m}^2/\text{g}$, more than twice the original $32 \text{ m}^2/\text{g}$ for TiO_2 , was observed after addition of 0.6 wt.% of cerium. Further increase of Ce amount up to 1.4 wt.% enhances the photocatalyst specific surface area only to $\sim 99 \text{ m}^2/\text{g}$. These results pretty follow the trend revealed in more detailed surface area and porous structure morphology investigation of cerium doped titania in our previous work

[24], where higher amounts of cerium were added to titania. All the investigated textural properties (S_{BET} , S_{meso} , V_{micro} , V_{net}) increased with maximum at 6.3 wt.% Ce (3 mol.% Ce/ TiO_2). Further increase of cerium amount decreased all textural properties due to nucleation of CeO_2 [24]. Because these photocatalysts modified by low amount of cerium are prepared in the same way as the ones with high amount of cerium, we can safely presume the same (increasing) trend in the change of other textural properties (S_{meso} , V_{micro} , V_{net}) of the photocatalyst. The significant effect of ceria addition on the textural properties of the investigated photocatalysts can be attributed to microstructural changes caused by doping which is discussed in next paragraph.

3.3. Structural and microstructural properties

Structural and microstructural properties of explored photocatalysts evaluated from X-ray diffraction patterns (Fig. 2) are summarized in Table 2. From Fig. 2 it can be revealed that the parent TiO_2 as well as all explored cerium loaded titania photocatalysts comprise only pure anatase crystalline phase since in the patterns only anatase reflections can be identified. Diffraction peaks are strongly broadened due to small crystallite sizes and the effect increases with the cerium content. This is illustrated on the triplet of anatase reflections in the inset of Fig. 2. Any reflections from ceria crystalline phase or from other titania crystalline polymorphs such as rutile or brookite were not observed and the patterns fits were also excellent for data of high statistical quality (Fig. 3). For XRD data fitting the anatase crystallites were assumed to be spherical with diameter distributed according to the log-normal distribution [29]. The refined anatase crystallite-size distributions are depicted in Fig. 4. Considering the volume weighted TiO_2 anatase crystallite

Table 1
Specific surface area and absorption edge of investigated photocatalysts.

Photocatalyst	XRF Real content of cerium (wt.%)	Physisorption S_{BET} (m^2/g)	UV–vis Absorption edge (eV)
TiO_2 Evonik P25	0	50 ^a	3.39
TiO_2	0	32	3.19
0.6 wt.% Ce/ TiO_2	0.56	76	3.14
1.2 wt.% Ce/ TiO_2	1.19	93	3.00
1.4 wt.% Ce/ TiO_2	1.39	99	2.97

^a Average value given by manufacturer $50 \pm 15 \text{ m}^2/\text{g}$.

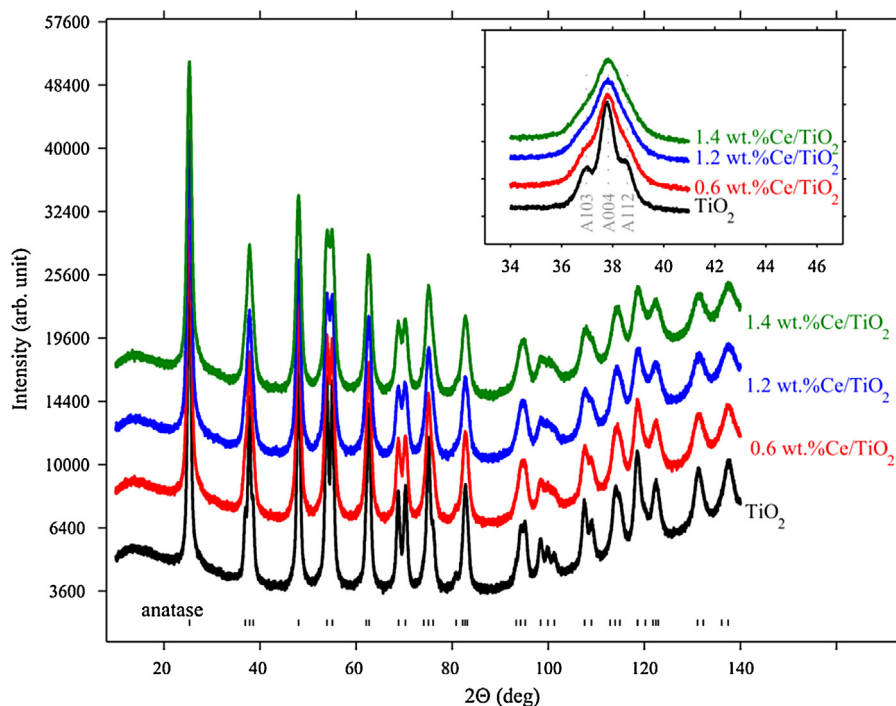


Fig. 2. XRD patterns of investigated TiO_2 and Ce/TiO_2 photocatalysts.

size (Table 2), which was also determined for Ce/TiO_2 photocatalysts in our previous work [24], one can see monotonous decrease of anatase crystallite size with the cerium loading (i.e. from 17.9 nm for parent TiO_2 to 9.8 nm for 1.4 wt.% Ce/TiO_2). The decreasing anatase crystallite size with increasing cerium content agrees with the evolution of size distributions in Fig. 4. The decreasing trend within 0–1.4 wt.% of cerium in TiO_2 fits quite well the previously observed trend for 0.28–10 mol.% of Ce [24] (0.6–21.1 wt.% Ce) when the volume weighted TiO_2 anatase crystallite size was

decreasing up to 3 mol.% of Ce (6.3 wt.% Ce). Thus, the inhibiting effect of cerium on the growth of TiO_2 crystallites for the cerium content of 0–1.4 wt.% can be proved. The decreasing anatase crystallite size also correlates with the increasing surface area of the photocatalysts. Both correlations are shown in Fig. 5.

Concerning the possible incorporation of Ce^{4+} ions into TiO_2 lattice, which may be the cause of the inhibiting effect of cerium on the TiO_2 crystallites growth, this effect can be observed from refined anatase lattice parameters and the expansion of anatase

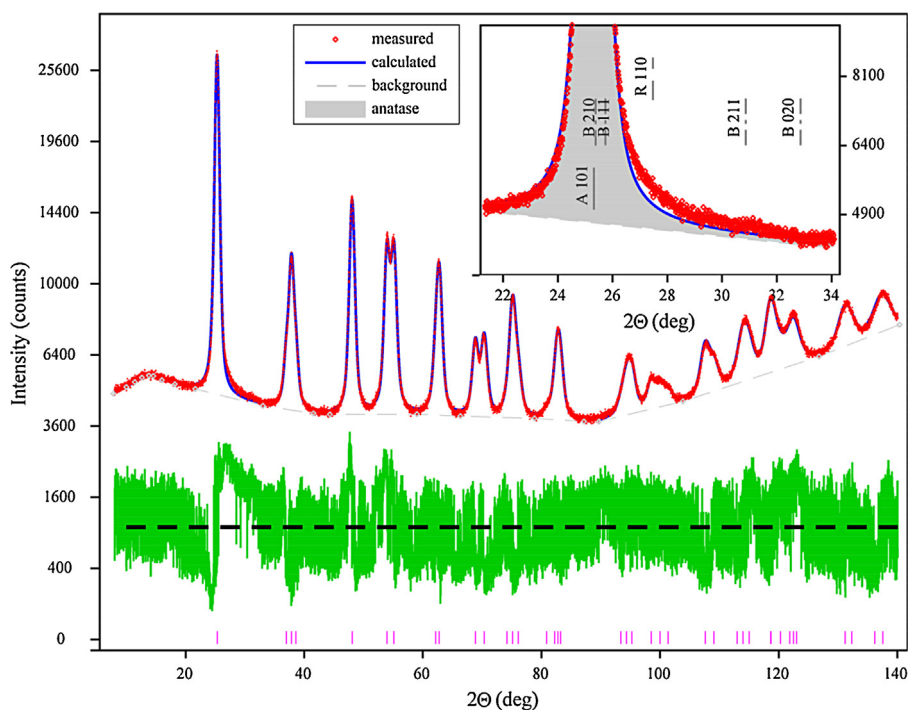


Fig. 3. Full XRD pattern fit of 1.2 wt.% Ce/TiO_2 photocatalyst. Possible reflection positions of different TiO_2 phases (A – anatase, B – brookite, R – rutile) are shown in the inset.

Table 2
Structural and microstructural properties of investigated photocatalysts evaluated from XRD.

Photocatalyst	Crystallite-size and crystallite-size distribution				Lattice parameters and cell volume		
	M (nm)	σ	$\langle D \rangle_V$ (nm)	$\langle D \rangle_A$ (nm)	a (Å)	c (Å)	V_{cell} (Å ³)
TiO ₂	9.85	0.413	17.9	15.1	3.78613	9.51447	136.388
0.6 wt.% Ce/TiO ₂	7.97	0.349	12.2	10.8	3.78689	9.51254	136.415
1.2 wt.% Ce/TiO ₂	6.65	0.349	10.2	9.0	3.78709	9.51253	136.429
1.4 wt.% Ce/TiO ₂	6.83	0.323	9.8	8.9	3.78733	9.51185	136.437

M – median of the log-normal anatase crystallites size distribution.

σ – multiplicative standard deviation of the log-normal anatase crystallite-size distribution.

$\langle D \rangle_V$ – volume weighted anatase crystallite size.

$\langle D \rangle_A$ – area weighted anatase crystallite size.

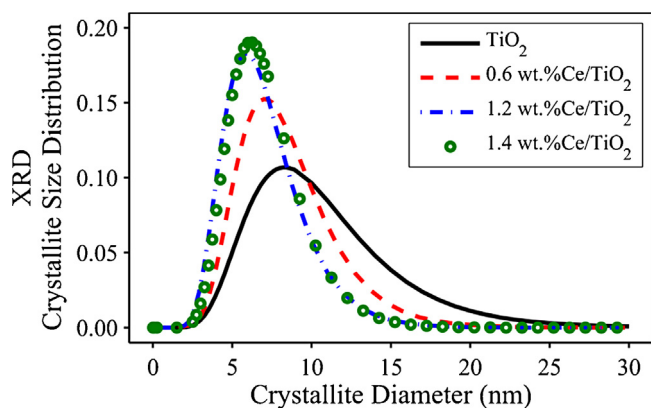


Fig. 4. Crystallite size distributions as determined from XRD analysis.

cell volume. Since Ce⁴⁺ ions are larger than Ti⁴⁺ ions (0.92 Å and 0.68 Å, respectively) [36], when Ce⁴⁺ ions are incorporating into TiO₂ lattice the anatase cell volume is expanding, accompanied with its limitation while reaching titania lattice saturation by Ce⁴⁺ ions or, e.g. forming some amorphous/crystalline phase. Despite of the anatase cell volume is only slightly extending with increasing cerium loading within 0.6–1.4 wt.% of Ce as evident from Table 2, it corresponds with the trend observed for higher Ce loadings, indicating the possible cerium ions incorporation into titania (Fig. 6).

3.4. Optical properties

The UV–vis diffuse reflectance spectra of all investigated photocatalysts were taken in order to find out their spectral response. As expected the addition of cerium significantly influenced the

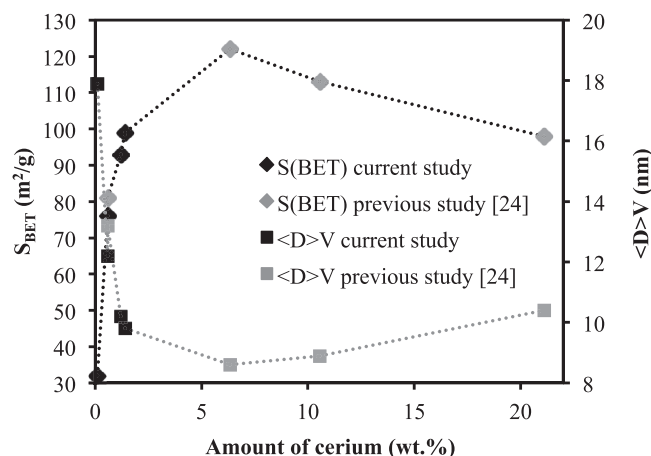


Fig. 5. Correlations between the Ce amount, anatase crystallite size and photocatalysts surface area.

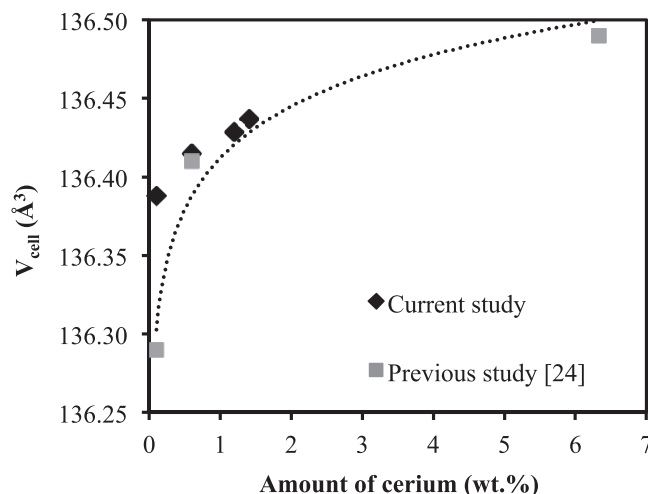


Fig. 6. Dependence of the anatase cell volume on the Ce amount added. The discrepancy in the anatase cell volume for pure TiO₂ in current and previous study is caused by the quality of fitted XRD data.

absorption properties of the photocatalysts, the spectra shifted toward the visible region with increasing amount of cerium (Fig. 7). All the prepared photocatalysts have intense characteristic band around 3.1 eV compared to the commercial TiO₂ Evonik P25 with characteristic band around 4.0 eV. The absorption edges of the photocatalysts were evaluated from the reflectance spectra (Fig. 8)

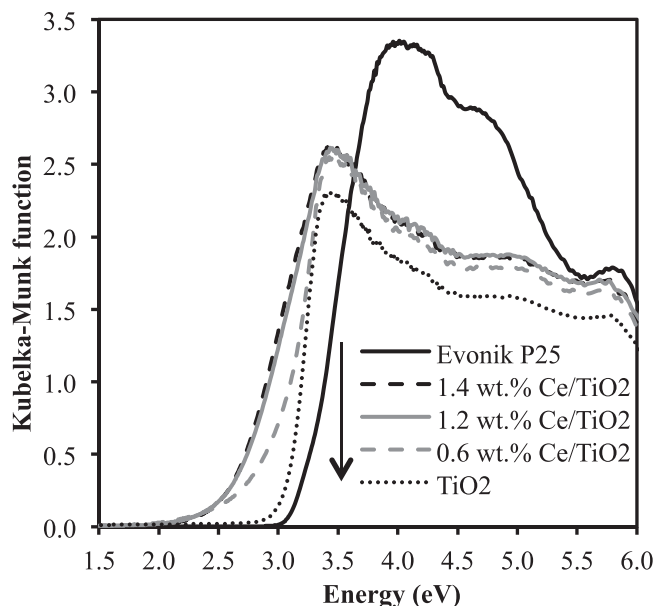


Fig. 7. UV–vis DRS spectra of investigated photocatalysts.

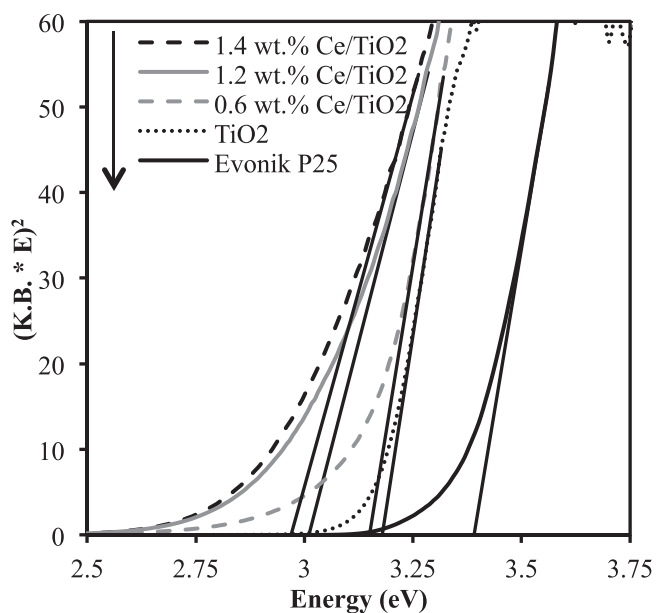


Fig. 8. Determination of the absorption edges of investigated photocatalysts.

and the exact numbers are shown in Table 1. The band gap energy of the photocatalyst is an important characteristic in photocatalysis. The theoretical minimal energy/wavelength of the photon capable to generate electron-hole pair in the photocatalyst is given by the band gap energy. The value of prepared TiO₂ absorption edge was 3.19 eV, which can be attributed to the band gap of pure anatase. The addition of cerium led to the decrease of absorption edge from 3.19 eV to 2.97 eV. The dependence of the absorption edge on the different loading of cerium is shown in Fig. 9. It can be seen that this dependence is linear within 0.6–1.4 wt.% of Ce and the decrease of the absorption edge is more pronounced than at higher cerium loadings. The decrease of absorption edge energy after addition of cerium was already published [37–39], but the exact explanation is still matter of discussion. Although, the lowering the band gap energy by doping is a desirable effect, the invoked changes in the reduction/oxidation potential of reaction have to be also taken into account.

3.5. The photocatalytic decomposition of ammonia

We decided to follow up the kinetics of NH₃ decomposition under UV light by the analysis of the formed H₂, which can be

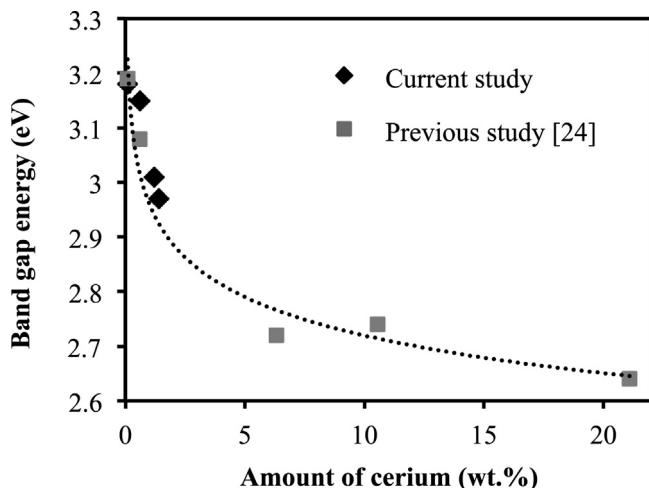


Fig. 9. Correlation between the Ce amount and the band gap energy.

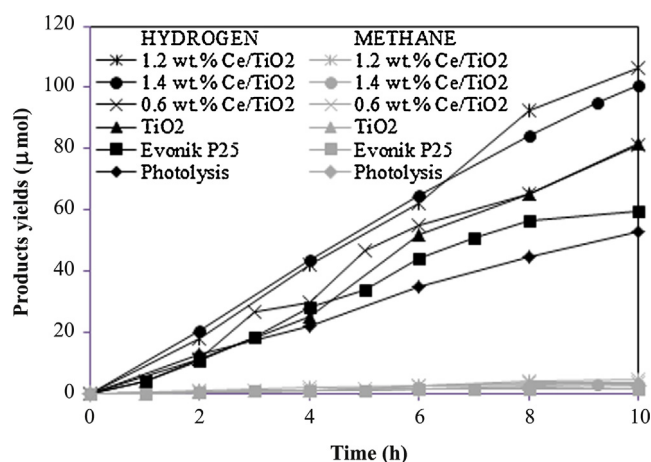


Fig. 10. Dependence of hydrogen and methane yields on the irradiation time over all investigated photocatalysts and in the case of photolysis.

easily analyzed by GC. First of all, blank tests were performed. We observed that hydrogen was not formed from an aqueous suspension of photocatalyst in the absence of NH₃, indicating that photocatalytic water splitting did not occur. The hydrogen was also not detected from an aqueous suspension of photocatalyst in the absence of UV irradiation. Finally, hydrogen was also not formed from ammonium hydroxide solution with photocatalyst in the dark. The addition experiments revealed that no nitrous oxide is produced during the photocatalytic decomposition of ammonia. In contrast to this, the decomposition of ammonium hydroxide solution under UV light without the catalyst (photolysis of ammonia) proceeds under given experimental conditions. These facts confirmed that the only source of hydrogen is ammonia and that the UV initiated decomposition of ammonia proceeds by photocatalytic and photochemical pathways according to the same Eq. (2).



The effect of irradiation time on the formation of hydrogen in the photocatalytic decomposition of ammonia was investigated over TiO₂ as well as over TiO₂ photocatalysts loaded with different amount of cerium over a period of 0–10 h.

The hydrogen yields over all examined photocatalysts and in case of photolysis are shown in Fig. 10. The nitrogen was also generated but due to not entirely gas tight valve system on GC the amount of generated nitrogen could not be reproducibly analyzed.

Against all expectation, there was a second product detected. The later product does not come from the photocatalytic decomposition of ammonia but obviously its yield is rising with the irradiation time. This compound was identified as methane and its concentration increased during the experiment to the maximal value of 4 μmol. The comparison of methane generation with the hydrogen formation over all photocatalysts is shown in Fig. 10. We can see that the methane yields were approximately 30 times lower than hydrogen. The first idea was that the methane comes from carbon dioxide adsorbed on the surface of the photocatalysts which was photocatalytically reduced to methane. But due to detection of methane also in photolysis, where no catalyst is present, the original idea had to be revised. The source of carbon which is eventually converted into methane comes not only from the adsorbed carbon species on the photocatalyst but also from the walls of the reactor. This assumption confirms the lower methane yields in presence of commercial TiO₂ Evonik P25. This catalyst is “very light” and when suspended in aqueous solution it creates “milky” suspension. Due to vigorous stirring the suspension splashes on the walls of the reactor and covers them with non-homogeneous white layer of TiO₂. This

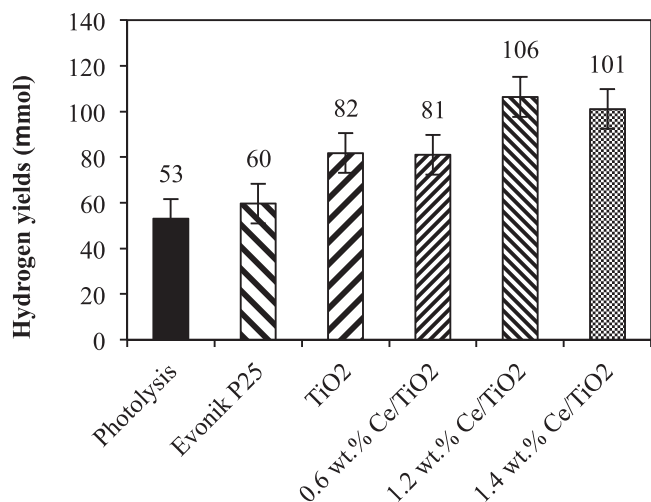


Fig. 11. Hydrogen yields over each investigated photocatalyst and in the case of photolysis after 10 h irradiation. Conditions: 10 h of irradiation, 8 W Hg lamp (254 nm), 100 ml of NH₄OH, 0.1 g of the photocatalyst.

layer of Evonik P25 partially blocks the UV irradiation from reaching the walls and so interacting with any carbon species present there. The rate of methane creation is slower with time due to more and more covered up reactor wall.

The other possible source of CH₄ can be the silicon glue used for fixing the quartz glass tube into the stainless steel cover. Recently, we have found out that the silicon glue is highly unstable under UV light. Even though the manufacturer says it is stable. The silicon glue is releasing different amounts of several organic compounds along with methane. We also cannot completely exclude the residua of dissolved CO₂ in the aqueous solution although the solution was purged by argon before reaction. Moreover, some small residues of the catalysts from previous experiments could be present in the reactor, especially in sintered glass frit used in gas feed.

We can conclude that the evolution of methane during experiments can be from several different sources and reasons. Generally, these observations imply that it is extremely important to be careful with interpretation of results of photocatalytic experiments with very low initial concentrations of pollutants because some misleading can be easily observed.

The hydrogen yields from longer time period (10 h) were chosen for the comparison of an individual photocatalytic performance because these yields were higher and thus less loaded by error and more reliable. The effect of cerium doping on the photocatalytic activity of prepared photocatalyst is shown in Fig. 11. The most active photocatalyst was the one with 1.2 wt.% of cerium. This correlates with our previous results where the photocatalyst with low amount of cerium (0.6 wt.%) was the most active one for photocatalytic reduction of CO₂ [24].

Photocatalytic reaction is a very complex process and the photocatalytic activity of the photocatalyst is being influenced by several aspects such as the band gap energy, surface area and surface properties and the most importantly electrons and holes energy levels. The addition of cerium led to positive increase of specific surface area and also to a positive decrease of band gap energy (Table 1). The knowledge of nanoparticles work function can help us to predict the photocatalytic activity of the photocatalysts. It was experimentally revealed that a different Ce loading in TiO₂ nanoparticles crucially affects the energy of holes in valence band and especially electrons in conduction band and these properties directly influence the ammonia photodecomposition. Fig. 12 shows an apparent correlation between the yields of hydrogen after 10 h of irradiation and the work function of each catalyst. There is an optimal value (the

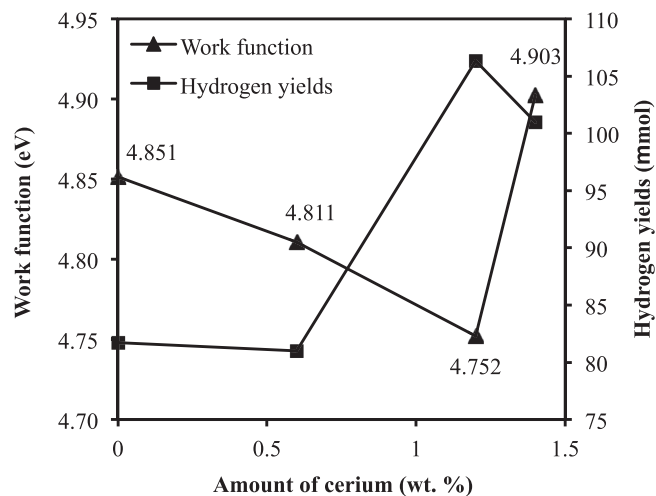


Fig. 12. Correlation between the work function and the photocatalytic activity of investigated photocatalysts.

lowest) of work function which correlates with the highest yield of hydrogen formed from the photocatalytic decomposition of ammonia. It is also in agreement with our previous results over cerium doped TiO₂ and ZnS/MMT photocatalysts tested in the CO₂ photocatalytic reduction [24,40]. The photocatalytic decomposition of ammonia is conducted via generated electrons and the 1.2 wt.% Ce/TiO₂ photocatalyst releases those electrons most easily (work function is 4.752 eV). Simply said, the work function measurement seems to be a very helpful tool for estimating the energy shift of valence and conduction bands of prepared catalysts.

For the ammonia photocatalytic decomposition the energy of electron formation in conduction band must be higher than N₂/NH₄OH reduction potential and the hole energy in valence band must be lower than OH⁻ oxidation potentials. TiO₂ is a direct wide band gap semiconductor ($E_g = 3.2$ eV), hence it absorbs only in the UV range, but it possesses a strongly reducing conduction band ($E_{CB} = -0.29$ V versus the NHE) [41]. The reason why prepared TiO₂ catalyst has significantly higher activity in photocatalytic generation of hydrogen than commercial Evonik P25 can be in different phase composition (prepared TiO₂: 100% anatase; Evonik P25: 80% anatase + 20% rutile [42]). The rutile phase presented in Evonik P25 has a low level of the conduction band which is insufficient for formation of H₂ (reduction of protons) [22]. The addition of Ce to TiO₂ should result in changing the band gap and the absorption edge energies and these changes were also experimentally demonstrated (see Fig. 8). However, it is always difficult to predict separately the shift of conduction and valence band energies, which are extremely important with respect to required oxidation and reduction potentials.

The nanoparticles work function for different Ce contents shown in Fig. 12 can help us to elucidate the shifts of conduction as well as valence bands. For simplicity the Fermi level on nanoparticle surface is supposed to be pinned to the middle of the nanoparticle band gap. Deriving from Fig. 8, Table 1 and Fig. 12, we can estimate that the energy of electrons formation on the conduction band edge is -3.256 eV, while the valence band edge is -6.446 eV for pure TiO₂ (Fig. 13). For 0.6 wt.% Ce/TiO₂ the energy of electrons on the conduction band edge decreases only about approximately 15 meV, while the valence band edge shifts up by 64 meV. The shift is very small because the difference both the work function of TiO₂ and 0.6 wt.% Ce/TiO₂ (4.851 eV and 4.811 eV, respectively) and their absorption edge (3.19 eV and 3.14 eV, respectively) is infinitesimal. Further increase of Ce content up to 1.2 wt.% led to a small conduction band increase (15 meV), whereas the valence band edge shifts

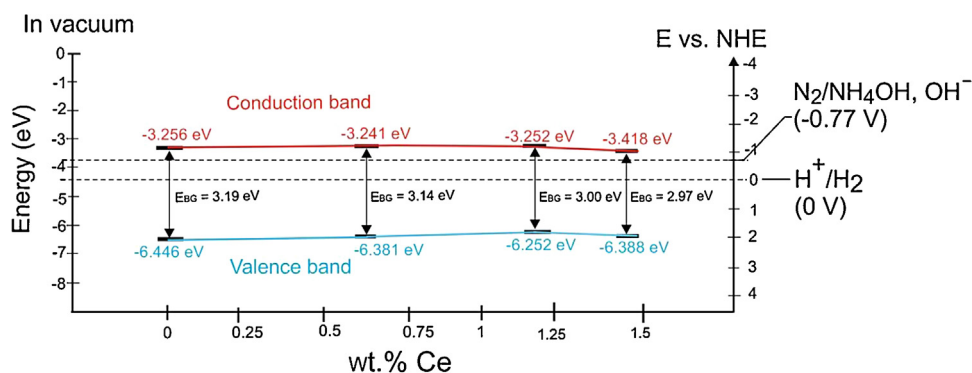


Fig. 13. Illustration of the shifts of energies of electrons and holes formation in conduction and valence bands in dependence on the Ce amount.

up by 129 meV. For 1.4 wt.% Ce/TiO₂ the conduction band edge as well as the valence band edge decreased by 229 eV and 136 eV, respectively, in comparison with 1.2 wt.% Ce/TiO₂. These shifts are depicted in Fig. 13. The higher level of the conduction band is more effective for the N₂/NH₄OH changes. It can be concluded that for 1.2 wt.% Ce/TiO₂ photocatalyst the carriers have the most favorable potentials for the photocatalytic decomposition of ammonia.

For better comparability of photocatalytic activity of the prepared catalysts, the kinetic constants were used. Since other possible reaction products of NH₃ decomposition (NO₃⁻, NO₂⁻ and N₂O) were not detected, the UV initiated ammonia decomposition is described by Eq. (2) generating N₂ and H₂. Assuming that both photocatalytic and photochemical ammonia decomposition proceeds parallel and can both be described by 1st order rate law, the total rate of ammonia decay is equal to the sum of the ammonia decrease by photocatalytic and photochemical pathways and is also described by 1st order rate law.

Unfortunately, we were unable to measure the decrease of ammonia concentration. The method using Nessler reagent was used for determination of ammonia content, but it was found out that the ammonia adsorbs on the catalyst which had to be removed (filtered, centrifuged) for the absorbance measurements. Therefore, the main component, the conversion was evaluated from, wasn't ammonia but generated hydrogen. Conversion of ammonia (4) was derived from hydrogen mass balance (3).

$$n_{H_2} = n_{H_2}^0 + \frac{3}{2} n_{NH_3}^0 \cdot X_{NH_3} \quad (3)$$

$$X_{NH_3} = \frac{\frac{2}{3} (n_{H_2} - n_{H_2}^0)}{n_{NH_3}^0} \quad (4)$$

where $n_{H_2}^0$, n_{H_2} , is the number of moles of H₂ at the beginning of reaction ($t=0$) and at different times during the photocatalytic reaction, respectively, $n_{NH_3}^0$ is the number of moles of NH₃ at the beginning of reaction ($t=0$) and X_{NH_3} is conversion of NH₃.

An integral form of material balance of batch reactor with ideal mixing working in isothermal isobaric regime was used for data processing:

$$\ln \frac{1}{1 - X_{NH_3}} = k \cdot t \quad (5)$$

where k is the kinetic constant (h⁻¹) and t is reaction time (h). Evaluation of the kinetic data (Fig. 14) confirmed that the reaction kinetics can be described by 1st order rate law. The values of complex kinetic constants k are listed in Table 3. The values of kinetic constants support the catalysts activity expressed by hydrogen yields (Fig. 10).

The observed different photocatalytic activity of parent TiO₂ and cerium doped TiO₂ photocatalysts can be connected with several

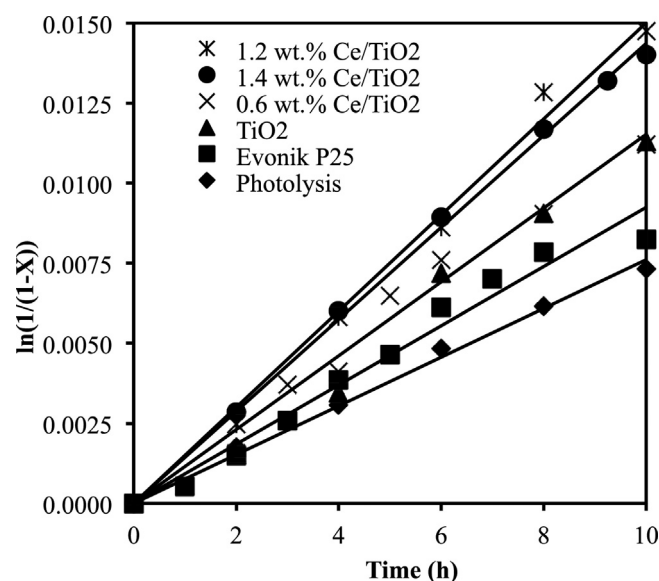


Fig. 14. Evaluation of complex kinetic constants (1st rate law) by the integral method for ammonia photocatalytic and photochemical decomposition.

factors such as (i) the specific surface area (determines the available surface active sites for the reaction), (ii) the value of absorption edge (defines the amount of photons that will be available for quantum conversion), (iii) work function. For (i), the Ce doped TiO₂ photocatalysts had higher surface areas, particularly photocatalysts with higher content of cerium (1.2 and 1.4 wt.% Ce) (S_{BET} , 93 m²/g and 99 m²/g, respectively) than pure TiO₂ or Evonik P25 photocatalyst areas (S_{BET} , 32 m²/g and 50 m²/g, respectively) (Table 1). For (ii), the band gap energy of 1.2 and 1.4 wt.% Ce photocatalyst was 3 eV and 2.97 eV, respectively, but the band gap energy of pure TiO₂ photocatalyst was 3.19 eV. For (iii), the lowest work function was measured for 1.2 wt.% Ce/TiO₂ 4.752 eV whereas the work function of pure TiO₂ was 4.851 eV.

Based on all results it is evident that the presence of Ce and its loading in titania plays the key role concerning the influence on

Table 3
Kinetic constants with statistic errors for all tested catalysts.

Catalyst/photolysis	Kinetic constant (h ⁻¹)
Photolysis	0.000761 ± 0.000014
Evonik P25	0.000925 ± 0.000028
TiO ₂	0.001116 ± 0.000041
0.6 wt.% Ce/TiO ₂	0.001153 ± 0.000034
1.2 wt.% Ce/TiO ₂	0.001501 ± 0.000033
1.4 wt.% Ce/TiO ₂	0.001437 ± 0.000014

textural (specific surface area), structural (phase composition) and microstructural (crystallite-size, size distribution, lattice parameters and cell volume) properties. The specific surface area of the photocatalysts enhances with increasing Ce loading in TiO₂ as a consequence of decreasing anatase crystallite size. But, in principal, these factors are not the main properties determining the catalyst efficiency for the photocatalytic ammonia decomposition. The band gap width and the energy of electrons and holes formation in CB and VB, respectively, have the determining role since these two parameters are directly connected with the reaction mechanism. The band gap energy determined from UV–vis and the nanoparticle work function determined by the contact potential difference measurements are the characteristics helping us to predict the energy of electrons in valence band and thus describe the electronic structure of the semiconductor photocatalysts (Fig. 13). Knowledge of valence and conduction bands energies allows us to forecast the photocatalytic efficiency for the studied photocatalytic reactions.

4. Conclusions

Cerium doped TiO₂ photocatalysts with different Ce loadings (0–1.4 wt.%) were prepared by the sol–gel method and for the first time examined for the ammonia photocatalytic decomposition. NH₃ was decomposed to H₂ and N₂ stoichiometrically and side reactions such deep oxidation to NO²⁻ and NO³⁻ did not occur under present conditions.

Prepared TiO₂ catalyst had significantly higher activity in the photocatalytic generation of hydrogen than commercial TiO₂ Evonik P25 because the rutile phase presented in TiO₂ Evonik P25 has a low level of the conduction band which is insufficient for formation of H₂ (reduction of protons). The modification of TiO₂ with cerium caused the incorporation of cerium ions into the TiO₂ lattice leading to the expansion of anatase cell volume and inhibition of anatase crystallites growth corresponding to the increase of specific surface area of the catalysts. The shift of spectral response of Ce-modified catalysts to the visible light region was observed and the decrease of absorption edge of photocatalysts with increasing Ce loading was detected.

The Ce modification of TiO₂ also influenced the photocatalytic hydrogen formation. The direct correlation between catalysts work function, band gap energy and hydrogen yields was found out. The optimal Ce content in TiO₂ anatase, which will maximally lower the band gap energy while keeping sufficient electron and hole potentials to enter the photocatalytic reaction, may be estimated to 1.2 wt.% of Ce.

Acknowledgements

This work has been elaborated in the framework of the following projects: “Opportunity for young researchers” (reg. no. CZ.1.07/2.3.00/30.0016) and “New creative teams in priorities of scientific research” (reg. no. CZ.1.07/2.3.00/30.0055), supported by Operational Programme Education for Competitiveness and co-financed by the European Social Fund and the state budget of the Czech Republic; the EU project “ENET” (reg. no. CZ.1.05/2.1.00/03.0069); the “National Feasibility Program I” (project LO1208 “TEWEP”) and the project SP2014/48 from Ministry of Education, Youth and Sports of the Czech Republic.

The work of Zdenek Matej is a part of activities of the Charles University Research Center “Physics of Condensed Matter and Functional Materials”.

References

- [1] C.C. Delwiche, Denitrification, Nitrification, and Atmosphere Nitrous Oxide, John Wiley and Sons, New York, 1981.
- [2] G. Tchobanoglous, F.L. Burton, Wastewater Engineering Treatment, Disposal and Reuse, McGraw-Hill, New York, 1991.
- [3] S. Shibuya, S. Aoki, Y. Sekine, I. Mikami, Appl. Catal. B 138–139 (2013) 294–298.
- [4] X. Zhu, M.A. Nanny, E.C. Butler, J. Photochem. Photobiol. A 185 (2007) 289–294.
- [5] X. Zhu, M.A. Nanny, E.C. Butler, Water Res. 42 (2008) 2736–2744.
- [6] B. Boulinguez, A. Bouzaza, S. Merabet, D. Wolbert, J. Photochem. Photobiol. A 200 (2008) 254–261.
- [7] E.-M. Bensen, S. Schroeter, H. Jacobs, J.C. Broekaert, Chemosphere 35 (1997) 1431–1445.
- [8] K.-M. Bark, H.-S. Lee, W.-H. Cho, H.-R. Park, Bull. Korean Chem. Soc. 29 (2008) 869–872.
- [9] S. Yamazoe, Y. Hitomi, T. Shishido, T. Tanaka, Appl. Catal. B 82 (2008) 67–76.
- [10] M. Kaneko, H. Ueno, R. Saito, J. Nemoto, Catal. Lett. 137 (2010) 156–162.
- [11] Y. Shavisi, S. Sharifnia, S.N. Hosseini, M.A. Khadivi, J. Ind. Eng. Chem. 20 (2014) 278–283.
- [12] M. Zendezhaban, S. Sharifnia, S.N. Hosseini, Korean J. Chem. Eng. 30 (2013) 574–579.
- [13] Y. Shavisi, S. Sharifnia, M. Zendezhaban, M.L. Mirghavami, S. Kakehazar, J. Ind. Eng. Chem. 20 (2014) 2806–2813.
- [14] M. Altomare, G.L. Chiarello, A. Costa, M. Guarino, E. Selli, Chem. Eng. J. 191 (2012) 394–401.
- [15] M. Altomare, E. Selli, Catal. Today 209 (2013) 127–133.
- [16] L.A. Pretzer, P.J. Carlson, J.E. Boyd, J. Photochem. Photobiol. A 200 (2008) 246–253.
- [17] H.H. Ou, C.H. Liao, Y.H. Liou, J.H. Hong, S.L. Lo, Environ. Sci. Technol. 42 (2008) 4507–4512.
- [18] H.-H. Ou, M.R. Hoffmann, C.-H. Liao, J.-H. Hong, S.-L. Lo, Appl. Catal. B 99 (2010) 74–80.
- [19] L. Kowalczyk, M.I. Szykowska, Chem. Pap. 66 (2012) 607–611.
- [20] Q. Li, K. Domen, S. Naito, T. Onishi, K. Tamaru, Chem. Lett. 3 (1983) 321–324.
- [21] J. Nemoto, N. Gokan, H. Ueno, M. Kaneko, J. Photochem. Photobiol. A 185 (2007) 295–300.
- [22] H. Kominami, H. Nishimune, Y. Ohta, Y. Arakawa, T. Inaba, Appl. Catal. B 111 (2012) 297–302.
- [23] H. Yuzawa, T. Mori, H. Itoh, H. Yoshida, J. Phys. Chem. C 116 (2012) 4126–4136.
- [24] L. Matějová, K. Kočí, M. Reli, L. Čapek, A. Hospodková, P. Peikertová, Z. Matěj, L. Obalová, A. Wach, P. Kuštrowski, A. Kotarba, Appl. Catal. B 152 (2014) 172–183.
- [25] L. Matějová, T. Cajthaml, Z. Matěj, O. Benada, P. Klusón, O. Šolcová, J. Supercrit. Fluids 52 (2010) 215–221.
- [26] L. Matějová, V. Valeš, R. Fajgar, Z. Matěj, V. Holý, O. Šolcová, J. Solid State Chem. 198 (2013) 485–495.
- [27] S.J. Gregg, K.S.W. Sing, Adsorption, Surface Area and Porosity, Academic Press, New York, 1982.
- [28] S. Brunauer, P.H. Emmett, E. Teller, J. Am. Chem. Soc. 60 (1938) 309–319.
- [29] P. Scardi, M. Leoni, Acta Crystallogr. Sect. A: Found. Crystallogr. 58 (2002) 190–200.
- [30] Z. Matěj, R. Kužel, MStruct – Program/Library for MicroStructure Analysis by Powder Diffraction, 2009.
- [31] Z. Matej, R. Kuzel, L. Nichtova, Powder Diffr. 25 (2010) 125–131.
- [32] Z. Matěj, L. Matějová, R. Kužel, Powder Diffr. 28 (2013) 161–183.
- [33] M. de los Milagros Ballari, R. Brandi, O. Alfano, A. Cassano, Chem. Eng. J. 136 (2008) 50–65.
- [34] M. de los Milagros Ballari, R. Brandi, O. Alfano, A. Cassano, Chem. Eng. J. 136 (2008) 242–255.
- [35] K. Koci, L. Obalova, D. Placha, Z. Lacny, Collect. Czech. Chem. Commun. 73 (2008) 1192–1204.
- [36] J. Fang, X. Bi, D. Si, Z. Jiang, W. Huang, Appl. Surf. Sci. 253 (2007) 8952–8961.
- [37] Y. Jiang, N. Bahlawane, J. Alloys Compd. 485 (2009) L52–L55.
- [38] Y.H. Xu, Z.X. Zeng, J. Mol. Catal. A: Chem. 279 (2008) 77–81.
- [39] F.B. Li, X.Z. Li, M.F. Hou, K.W. Cheah, W.C.H. Choy, Appl. Catal. A 285 (2005) 181–189.
- [40] K. Kočí, L. Matějová, O. Kozák, L. Čapek, V. Valeš, M. Reli, P. Praus, K. Šafářová, A. Kotarba, L. Obalová, Appl. Catal. B 158 (2014) 410–417.
- [41] A. Mills, R.H. Davies, D. Worsley, Chem. Soc. Rev. 22 (1993) 417–425.
- [42] L. Matějová, K. Kočí, M. Reli, L. Čapek, V. Matějka, O. Šolcová, L. Obalová, Appl. Surf. Sci. B 285 (2013) 688–696.